Layer-Dependent Nonlinear Absorption and Refraction of ReX_2(X = Se, S) Films Grown by Chemical Vapor Deposition

Yanqing Ge,[1,‡] Chunhui Lu,[1,‡] Qiyi Zhao,[2] Mingwei Luo,[1] Yuqi Liu,[1] Taotao Han,[1] Yixuan Zhou,[1,*] and Xinlong Xu[1,†]

[1] *State Key Laboratory of Photoelectric Technology and Functional Materials, International Collaborative Center on Photoelectric Technology and Nano Functional Materials, Institute of Photonics & Photon-Technology, School of Physics, Northwest University, Xi'an 710069, China*

[2] *School of Science, Xi'an University of Posts and Telecommunications, Xi'an 710121, China*

(Received 3 May 2022; revised 13 July 2022; accepted 18 August 2022; published 20 September 2022)

Recent studies have revealed that atomically thin two-dimensional (2D) materials exhibit outstanding nonlinear optical (NLO) properties compared with traditional NLO crystals, which provides great potential in numerous photonic devices such as integrated nonlinear photonic chips and modulators. However, the evolution of NLO response with layer number and pump intensity of various 2D materials remains unclear, but offers a basis for hunting powerful NLO materials. Herein, controllable synthesis of a series of ReX_2 (X = Se, S) films with different numbers of layers is achieved by chemical vapor deposition. Z-scan techniques are used to investigate the nonlinear absorption coefficient (β) and nonlinear refractive index (n_2). Empirically, the absolute values of both β and n_2 show a downtrend as the power exponential function with the layer and pump intensity. The NLO parameters of $ReSe_2$ film are $\beta \sim 4156$ cm/GW and $n_2 \sim 1.819 \times 10^{-10}$ cm^2/W, which are more significant than those of ReS_2 film ($\beta \sim 806$ cm/GW and $n_2 \sim 2.22 \times 10^{-11}$ cm^2/W). This result is ascribed to the smaller band gap, higher carrier density, and larger ground-state absorption of $ReSe_2$ than that of ReS_2, which is confirmed by the theoretical analysis of the band structure and a three-energy-level system. It is worth pointing out that the β values for ReX_2 films are 10–100 times larger than those of WS_2, $MoSe_2$, and $MoTe_2$. The n_2 values for ReX_2 films are 3–4 orders of magnitude larger than for traditional semiconductors such as GaAs and Si. Our results suggest that ReX_2 semiconductors are greatly anticipated in designing high-performance on-chip photonic devices.

DOI: 10.1103/PhysRevApplied.18.034050

I. INTRODUCTION

Compared with traditional optical materials, two-dimensional (2D) materials demonstrate superior optical and electronic properties, including ultrafast carrier dynamics (interband in the picosecond range, intraband in the femtosecond range), long lifetimes (greater than nanoseconds), and high electron mobility [1]. Furthermore, 2D materials have demonstrated stronger nonlinear optical (NLO) effects than traditional NLO crystals, such as β-BaB_2O_4, LiB_3O_5, $LiNbO_3$, and $KTiOPO_4$ [2–5]. In particular, a large nonlinear absorption coefficient (β) and nonlinear refractive index (n_2) are greatly anticipated in the continual miniaturization of photonic and optoelectronic devices [6,7]. Among these 2D materials, graphene [8,9], black phosphorus (BP) [10,11], and transition metal dichalcogenides (TMDs) [12,13] have been mostly investigated for their NLO properties. Graphene as a saturable absorber shows a broadband and intensity-dependent NLO absorption, but the relatively low nonlinear absorption coefficient ($\beta \sim -1.16 \times 10^2$ cm/GW at 800 nm) [14] and zero-band-gap feature severely prevent its application in optical switching [15]. As a powerful substitute for graphene, BP also exhibits a narrow and tunable band gap (0.3–2.2 eV) and giant NLO response ($\beta \sim -3460$ cm/GW at 800 nm) [10], but the poor air stability hinders its applications in ultrafast lasers [16]. With the great advancement in the synthesis of 2D materials, group VI TMDs, such as MoS_2 and WS_2, have shown a strong β in the approximately 10^2 cm/GW scale [9,13,14] and were successfully applied in mode lockers in ultrafast lasers at 1, 1.5, and 2 μm [17–19]. Despite the strong potential for multifunctional photonic devices, the manufacturing difficulty regarding size and layer is largely increased due to the band gap

*yxzhou@nwu.edu.cn

†xlxuphy@nwu.edu.cn

‡Yanqing Ge and Chunhui Lu contributed equally to this work.

variation from indirect to direct when the thickness is reduced from bulk counterpart to monolayer [20,21].

Compared with the typical group VI TMDs, ReX_2 ($X = $S, Se) shows a stable distorted 1T phase, which leads to a weak layer-dependent band gap (ReS_2 approximately 1.4 eV; $ReSe_2$ approximately 1.29 eV) [22]. This suggests that ReX_2 provides a platform to study nonlinear response and design corresponding nonlinear devices without the limitation of the monolayer. Up to now, the saturable absorption (SA) of both $ReSe_2$ and ReS_2 has been verified in various laser systems. For $ReSe_2$, mode-locking lasers have been achieved at the wavelength of 0.52 [23], 1.03 [23], 1.06 [24], 1.9 [25], and 2.0 μm [26]; passively Q-switched lasers were obtained at around 1.05 [27], 1.06 [28,29], 1.9 [22,30], and 2.0 μm [31]. For ReS_2, mode-locking lasers were obtained at the wavelength of 1.55 [32] and 1.56 μm [33–35]; Q-switched lasers have been obtained at 0.95 [36], 1.06 [36–38], 1.3 [38,39], 1.53 [40], and 1.55 μm [32]. These reports suggest a huge demand for the clarification of the nonlinear properties of ReX_2 as 2D NLO materials based on the following three key reasons: (I) Most of the reported ReX_2 saturable absorbers are prepared by liquid-phase exfoliation, which is usually accompanied by a larger nonlinear scattering and a stronger thermal effect. Compared with liquid-phase exfoliation, chemical vapor deposition (CVD) is a promising route for growing large-area and high-uniformity films. (II) The layer effect of ReX_2, considering the slightly variable band gap, is seldom included in the previous NLO studies. It is interesting to verify if these materials have an evolution of NLO response with different numbers of layers. (III) Previous works are mainly the proof-of-principle SA application at a below band-gap excitation. However, both nonlinear absorption and refractive index contrastive analysis of 2D NLO materials and the NLO mechanisms have rarely been explored.

Herein, a series of high-quality ReX_2 films with different numbers of layers are prepared by the CVD method, and the effects of the pump intensity and sample layer on the NLO absorption and refraction of ReX_2 are systematically studied by the Z-scan system. Under the excitation light of 800 nm, the β and n_2 of ReX_2 films decrease with the pump intensity and sample layer by a power-law function. For the NLO absorption, the β values of $ReSe_2$ and ReS_2 are -4156 cm/GW and -806 cm/GW, which are 10–100 times larger than those of WS_2, $MoSe_2$, and $MoTe_2$. For the NLO refractive index, the calculated n_2 of ReX_2 in a 10^{-11}–10^{-12} cm^2/W scale is 3–4 orders larger than those of Si and GaAs. Moreover, the absolute values of β and n_2 of $ReSe_2$ are more significant than those of ReS_2. Combining density functional theory and three-level analysis, it is verified that $ReSe_2$ has a smaller band gap, a higher carrier density, and a larger ground-state absorption. These results provide a guide of ReX_2 for the design and manufacture of high-performance nonlinear photonic devices.

II. ReX_2 FILM SYNTHESIS

The bottom-up synthesis of ReX_2 is carried out by the CVD method under a low-pressure atmosphere, as shown in Fig. 1(a). C-plane sapphires (1×1 cm^2) are chosen as substrates because of the high surface cleanliness and low energy barrier for the nucleation of 2D materials [41]. ReO_3 (Alfa Aesar, 99.9%) is selected as the Re precursor due to its fast nucleation rate and high crystal quality compared with Re metal and NH_4ReO_4 precursor [42]. Se and S powders are introduced to grow $ReSe_2$ and ReS_2, respectively. ReO_3 and Se (S) powders are located at the first and second temperature zones, respectively. The growth temperatures of the first and second zones are 600 and 300 °C (200 °C) to prepare $ReSe_2$ (ReS_2) films in a double-temperature furnace. Ar (80 sccm) and H_2 (10 sccm) act as the carrier gas to transport the vapor of ReO_3 and Se (S). The reaction time is 3 min at 600 °C. Here, the growth process can be divided into the following parts: (I) ReO_3 decomposes into Re_2O_7 and ReO_2 over 400 °C, which can be described by $ReO_3 \rightarrow Re_2O_7 + ReO_2$ [42]. (II) The vapor of Re_2O_7 and ReO_2 absorb and diffuse on the substrate till kinetic energy is lost [41]. (III) The S (Se) vapor is transferred by the carrier gas (Ar and H_2) and reacts with Re_2O_7 and ReO_2, which can be described by $Re_2O_7 + ReO_2 + H_2 + Se(S) \rightarrow ReSe_2(ReS_2) + H_2O + H_2Se(H_2S)$. (IV) The $ReSe_2$ (ReS_2) films grow layer by layer rapidly, and the layer number of the samples can be tuned by the vapor concentration at different deposition temperatures (more growth parameters for ReX_2 films are given in the Supplemental Material [43]).

Therefore, from an application perspective, 2D ReX_2 is more suitable for miniaturized photonic and optoelectronic devices compared with traditional NLO crystals. Although Re is expensive, the CVD method can prepare large-scale 2D layered ReX_2 films with only a little consumption of the precursor ReO_3. As a result, 2D ReX_2 still has advantages in NLO performance and cost for practical applications.

III. CHARACTERIZATION OF ReX_2 FILMS

The photographs of a series of centimeter-scale $ReSe_2$ films are shown at the bottom of Fig. 1(b). From left to right, the color of the sample becomes darker, indicating the increase of layer number. The optical microscopy image of the ultrathin $ReSe_2$ sample in Fig. 1(b) at the top is provided to show the surface morphology. The result indicates that the as-prepared large-area $ReSe_2$ film uniformly covers the sapphire substrate. Moreover, atomic force microscopy (AFM, Bruker, Dimension Icon) is used to measure the thicknesses of the $ReSe_2$ films. Figures 1(c) and 1(d) show the AFM image and the height profile of a $ReSe_2$ film approximately 1 nm thick. The thicknesses of the other films, approximately 2, 3, 20, and 30 nm, are also measured as shown in Fig. S1 (Supplemental Material

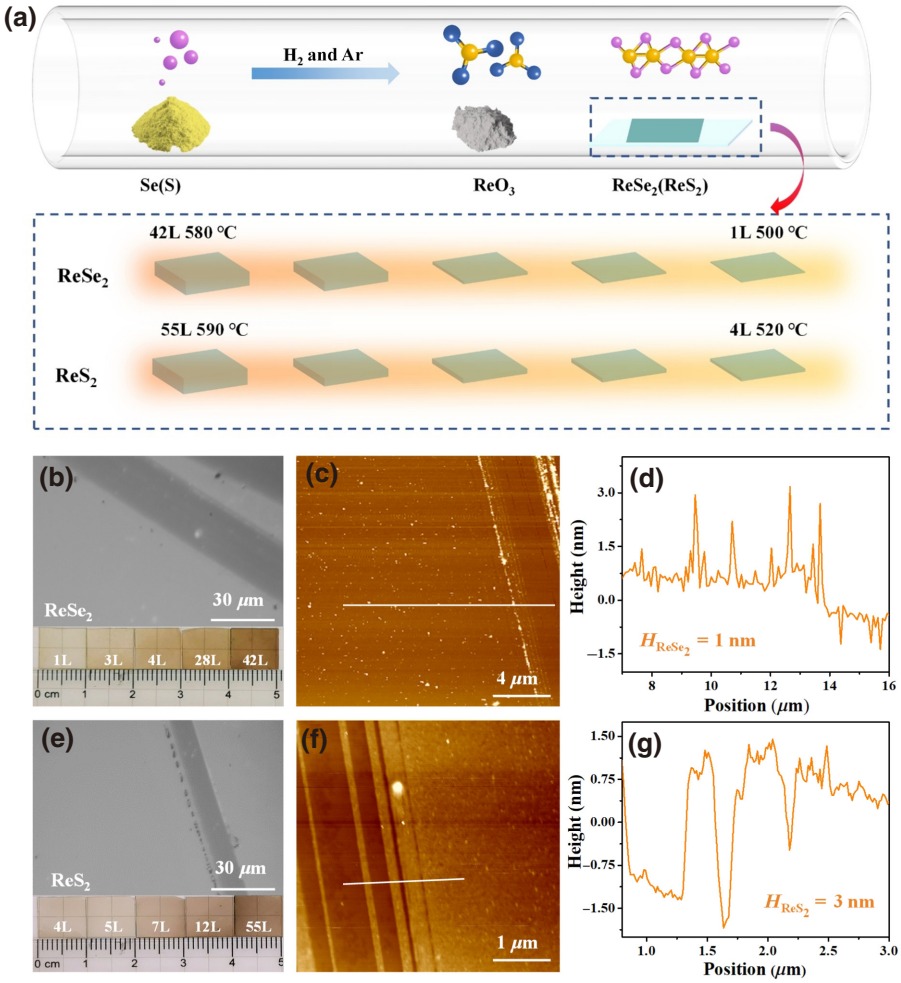

FIG. 1. (a) Schematic diagram of the preparation of ReX_2 films by CVD. (b) Bottom: photograph of the $ReSe_2$ films with different numbers of layers. Top: optical microscopy image of the ultrathin $ReSe_2$ film. (c) AFM image and (d) height profile of 1-nm $ReSe_2$ film. (e) Bottom: photograph of the ReS_2 films with different numbers of layers. Top: optical microscopy image of the 4L ReS_2 film. (f) AFM image and (g) height profile of 3-nm ReS_2 film.

[43]). The thickness of monolayer $ReSe_2$ is 0.71 nm [42]. Correspondingly, the layers of as-grown $ReSe_2$ films are 1L, 3L, 4L, 28L, and 42L, respectively. Similarly, a series of large-area uniform ReS_2 films with different numbers of layers can also be observed from the photograph and the optical microscopy image, as shown in Fig. 1(e). In addition, Fig. 1(f) shows the AFM image and the height profile of a ReS_2 film approximately 3 nm thick in Fig. 1(g), and more AFM results in Fig. S1 (Supplemental Material [43]) also confirm that the other films are approximately 3.7, 5, 9, and 40 nm thick. The corresponding layers of ReS_2 films are 4L, 5L, 7L, 12L, and 55L, where monolayer ReS_2 is approximately 0.73 nm [44]. These morphologic characterization results demonstrate that the ReX_2 films with different numbers of layers are all continuous and uniform. Meanwhile, the synthesized ReX_2 films are polycrystalline structures with the triclinic phase, confirmed by x-ray diffraction (XRD, Bruker, D8 Advance) as shown in Fig. S2 in the Supplemental Material [43].

To characterize the element composition and content information of ReX_2, x-ray photoelectron spectroscopy (XPS) is used. The full XPS spectrum of $ReSe_2$ is shown in Fig. 2(a), where the main element signals are Al, O, Re, and Se from both the sample and the sapphire substrate. From Figs. 2(b) and 2(c), the core-level peaks of Se $3d_{5/2}$, Se $3d_{3/2}$, Re $4f_{7/2}$, and Re $4f_{5/2}$ from divalent selenide ions (Se^{2-}) and tetravalent rhenium (Re^{4+}) are located at 54.9, 55.85, 41.9, and 44.3 eV [45], respectively. The calculated ratio of Re : Se is approximately 0.49, indicating that the $ReSe_2$ sample has a reasonable stoichiometric ratio. Similarly, the XPS spectrum also characterizes ReS_2 film, as shown in Fig. 2(d). Here, the main element signals are O, Re, S, and Al from the sample and the sapphire substrate. From Figs. 2(e) and 2(f),

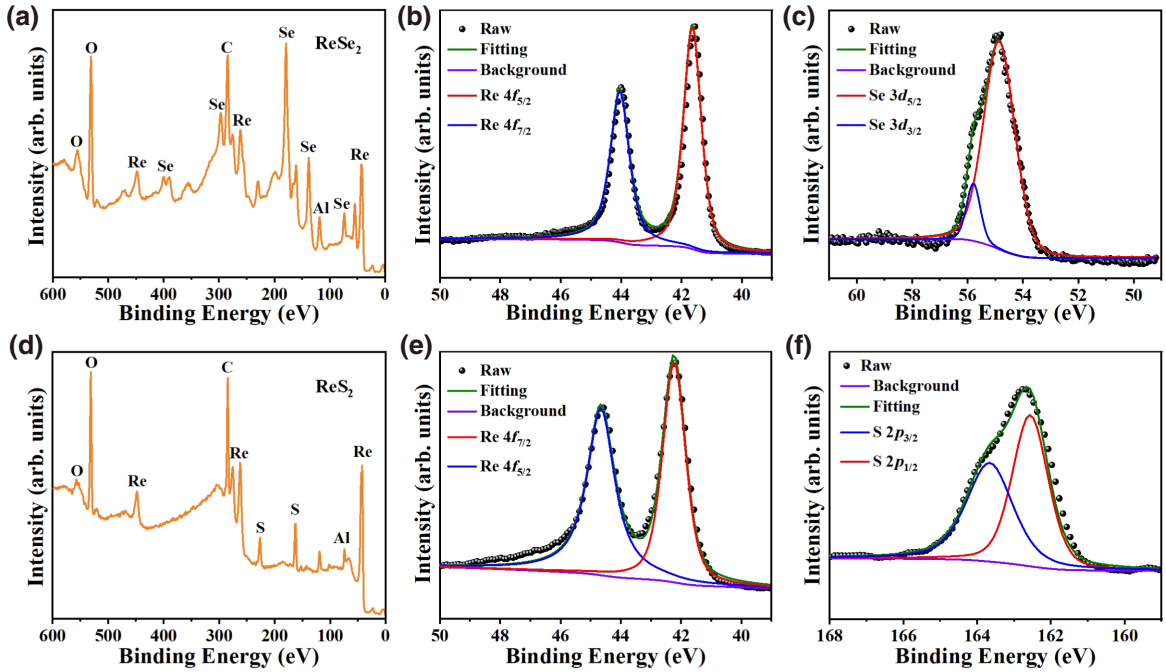

FIG. 2. Compositional analysis: (a) XPS survey spectrum of the $ReSe_2$ film, (b) Re 4*f*, and (c) Se 3*d* spectra; (d) XPS survey spectrum of ReS_2 film, (e) Re 4*f*, and (f) S 2*p* spectra.

the core level peaks of Re $4f_{7/2}$, Re $4f_{5/2}$, S $2p_{1/2}$, and S $2p_{3/2}$ from tetravalent rhenium (Re^{4+}) and divalent sulfide ions (S^{2-}) are located at 41.9, 44.3, 163.67, and 162.57 eV [38], respectively. The ratio of Re : S is calculated to be 0.49, indicating that the grown ReS_2 has a reasonable stoichiometric characteristic. The XPS characterization further proves the successful preparation of ReX_2 without evident vacancies.

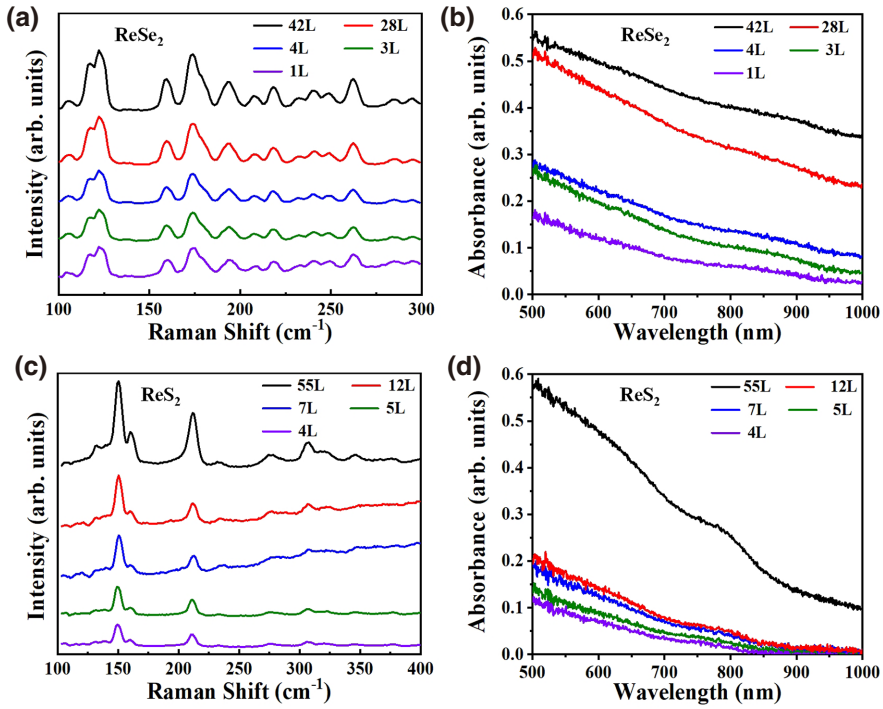

FIG. 3. (a) Raman and (b) linear absorption spectra of $ReSe_2$ films. (c) Raman and (d) linear absorption spectra of ReS_2 films.

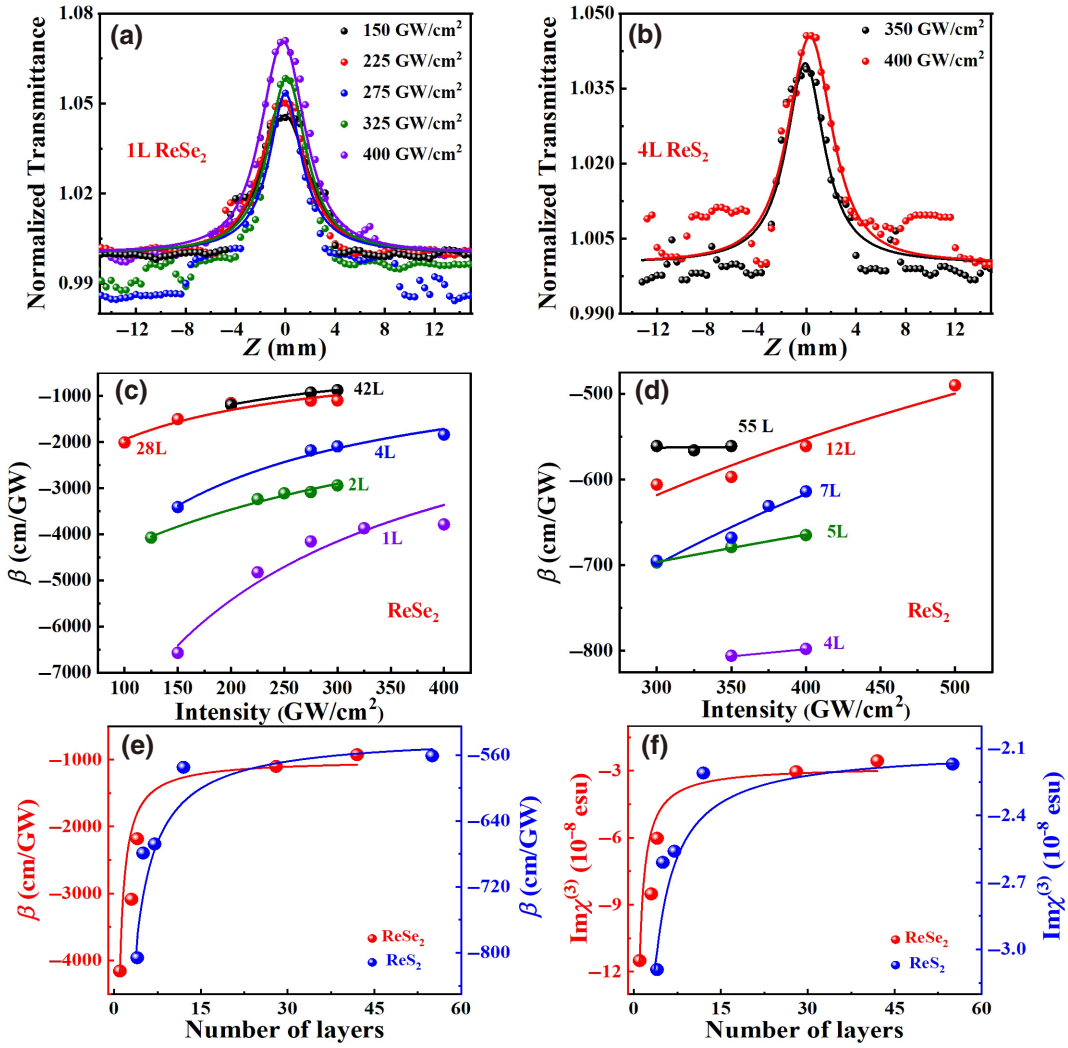

FIG. 4. OA Z-scan traces for (a) 1L $ReSe_2$ and (b) 4L ReS_2 films at different pump intensities. The values of β for (c) $ReSe_2$ and (d) ReS_2 films at different pump intensities. Layer dependent (e) β and (f) $\mathrm{Im}\chi^{(3)}$ values of ReX_2 films. The curves in (c)–(f) are fitted by the power law.

The Raman spectra of ReX_2 samples with different numbers of layers are collected and shown in Figs. 3(a) and 3(c). For $ReSe_2$ in Fig. 3(a), the characteristic Raman peak at 123 cm^{-1} can be ascribed to the in-plane (E_g-like) vibrational mode, and the peaks at 160 and 174 cm^{-1} are from the out-of-plane (Ag-like) vibrational modes [42]. Note that the other ten modes come from the low-symmetry structure of the sample [42], which further confirms the independence of band gap on layer. Similarly, for ReS_2 in Fig. 3(c), the characteristic Raman peaks at 212 and 150 cm^{-1} correspond to the A_g-like and E_g-like vibrational modes, respectively [46]. Compared with other TMDs, the Raman peaks of ReX_2 films have only a slight variation owing to the interlayer decoupling effect [42]. Moreover, the linear optical absorption properties of ReX_2 films are also studied using the ultraviolet-to-visible spectrometer (Ideaoptics R1). The absorption spectra of $ReSe_2$ and ReS_2 films with different numbers of layers are given in Figs. 3(b) and 3(d), respectively. Based on these results, the absorption coefficients of the ReX_2 samples at the wavelength of 800 nm are calculated and listed in Table S1 in the Supplemental Material [43].

IV. RESULTS AND DISCUSSION

A. Experimental method

The NLO absorption and refraction properties of the as-grown ReX_2 samples are explored by the Z-scan system with open aperture (OA) and closed aperture (CA) configurations, respectively. The self-built Z-scan system is equipped with a 35-fs Ti:sapphire laser at 800 nm, and the experimental setup is shown in Fig. S3 in the Supplemental Material [43].

TABLE I. NLO absorption parameters of 2D materials.

Sample	Number of layers	Laser Parameters	β (cm/GW)	Im$\chi^{(3)}$ (10^{-8} esu)	FOM$_{\mathrm{IM}}$ (10^{-14} esu cm)	Ref.
$ReSe_2$	1L	800 nm 35 fs 1 kHz	−4156	−11.5	17.5	This work
	3L		−3085	−8.51	15.8	
	4L		−2182	−6.02	12.3	
	28L		−1102	−3.04	25.3	
	42L		−878	−2.42	16.1	
ReS_2	4L		−806	−3.09	61.1	
	5L		−679	−2.61	34.8	
	7L		−668	−2.56	28.8	
	12L		−575	−2.21	39.1	
	55L		−561	−2.15	29.7	
WS_2	18L–20L	800 nm 40 fs 1 kHz	$-(397 \pm 40)$	$-(0.178 \pm 0.016)$	0.247 ± 0.023	[13]
WS_2	27.7 nm	800 nm 100 fs	$-(314.67 \pm 5.43)$	–	–	[15]
WS_2	131 nm	800 nm 35 fs 1 kHz	−76	−0.014	0.855	[14]
WS_2	20 μm	800 nm 35 fs 1 kHz	$-(5.1 \pm 0.26)$	$-(1.75 \pm 0.11) \times 10^{-3}$	–	[51]
Graphene	50 nm	800 nm 35 fs 1 kHz	−961.57	−0.24	3.1	[9]
Graphene	140 nm	800 nm 35 fs 1 kHz	−116	−0.028	1.36	[14]
MoS_2	65 nm	800 nm 35 fs 1 kHz	−136.13	−0.03	4.6	[9]
MoS_2	25 μm	1064 nm 25 ps 20 Hz	$-(3.8 \pm 0.59)$	$-(1.50 \pm 0.88) \times 10^{-3}$	–	[51]
MoS_2	68.98 nm	800 nm 1 kHz 35 fs	−60.38	-3.4×10^{-3}	0.078	[52]
$MoSe_2$	228 μm	800 nm 100 fs 100 kHz	−1.4	-9.1×10^{-5}	8.2	[12]
$MoTe_2$	64 nm	800 nm 1 kHz 35 fs	−166.33	-9.6×10^{-3}	0.287	[52]
BPNs	3.2–4.8 nm	800 nm 65 fs	−3460	$-(1.48 \pm 0.15)$	16.3 ± 2	[10]
BPNs	3.7 nm	800 nm 60 fs 1 kHz	$-(2.88 \pm 0.06) \times 10^{-2}$	-6.57 ± 0.15	7.24 ± 0.17	[53]
$PtSe_2$	0.5 nm	800 nm 150 fs	−4890	−2.06	–	[54]
Sb_2Se_3	84.3 nm	800 nm fs	−782	–	–	[55]
In_2Te_3	43 nm	800 nm 100 fs 1 kHz	−805.6	–	–	[56]
In_2Te_3	78 nm	800 nm 100 fs 1 kHz	−616.2	–	–	[56]

BPNs, black phosphorus nanosheets.

The β of the ReX_2 samples is measured by the OA Z-scan configuration, where normalized transmittance (T_{OA}) can be fitted by [47]

$$T_{\mathrm{OA}} = \sum_{m=0}^{\infty} \frac{[-\beta I_0 L_{\mathrm{eff}}/(1+Z^2/Z_0^2)]^m}{(m+1)^{3/2}} (m = 1, 2, 3), \quad (1)$$

where Z_0 and I_0 are the Rayleigh length of the laser beam and the on-focus incident intensity; $L_{\mathrm{eff}} = (1 - e^{-\alpha_0 L})/\alpha_0$ is the effective thickness of the ReX_2 films. Here, α_0 and L are the linear optical absorption coefficient and thickness of ReX_2 films, respectively.

Furthermore, the n_2 of ReX_2 films is obtained by the CA Z-scan technique. After dividing the corresponding OA signal to eliminate the influence of SA, the T_{CA} can be calculated by [47]

$$T_{\mathrm{CA}}(Z, \Delta\Phi_0) = 1 + \frac{4\Delta\Phi_0(Z/Z_0)}{[1+(Z/Z_0)^2][9+(Z/Z_0)^2]} \quad (2)$$

where $\Delta\Phi_0 = (2\pi/\lambda) n_2 I_0 L_{\mathrm{eff}}$ represents the on-axis phase shift and λ is the central wavelength of the femtosecond laser.

B. Nonlinear absorption properties of ReX_2 films

Firstly, the pump-intensity dependence of the nonlinear absorption is studied. As representations, Figs. 4(a) and 4(b) show the OA Z-scan traces of 1L $ReSe_2$ and 4L ReS_2 films at different pump intensities, respectively. Note that the reference sapphire substrate is also measured, and no nonlinear response is observed below the pump intensity of 1000 GW/cm^2, as shown in Fig. S4 in the Supplemental Material [43]. This suggests that the optical nonlinearity observed in our experiment comes only from the ReX_2 samples. For both 1L $ReSe_2$ and 4L ReS_2 films, the normalized transmittance increases with the pump intensity at the beam focus ($Z = 0$), indicating strong SA responses. Additionally, the NLO responses of the other $ReSe_2$ (3L, 4L, 28L, and 42L) and ReS_2 (5L, 7L, 12L, and 55L) films are also proved to be SA in Fig. S5 in the Supplemental Material [43]. Based on these Z-scan traces, the β values of $ReSe_2$ and ReS_2 films are calculated using Eq. (1) and summarized in Figs. 4(c) and 4(d), respectively. The absolute values of β decrease with pump intensity for both $ReSe_2$ and ReS_2, and the experimental data can be fitted by the power law [48] $\beta = A + B \times (1/I)$ (A and B are fitting parameters). Because the photon energy (1.55 eV) is

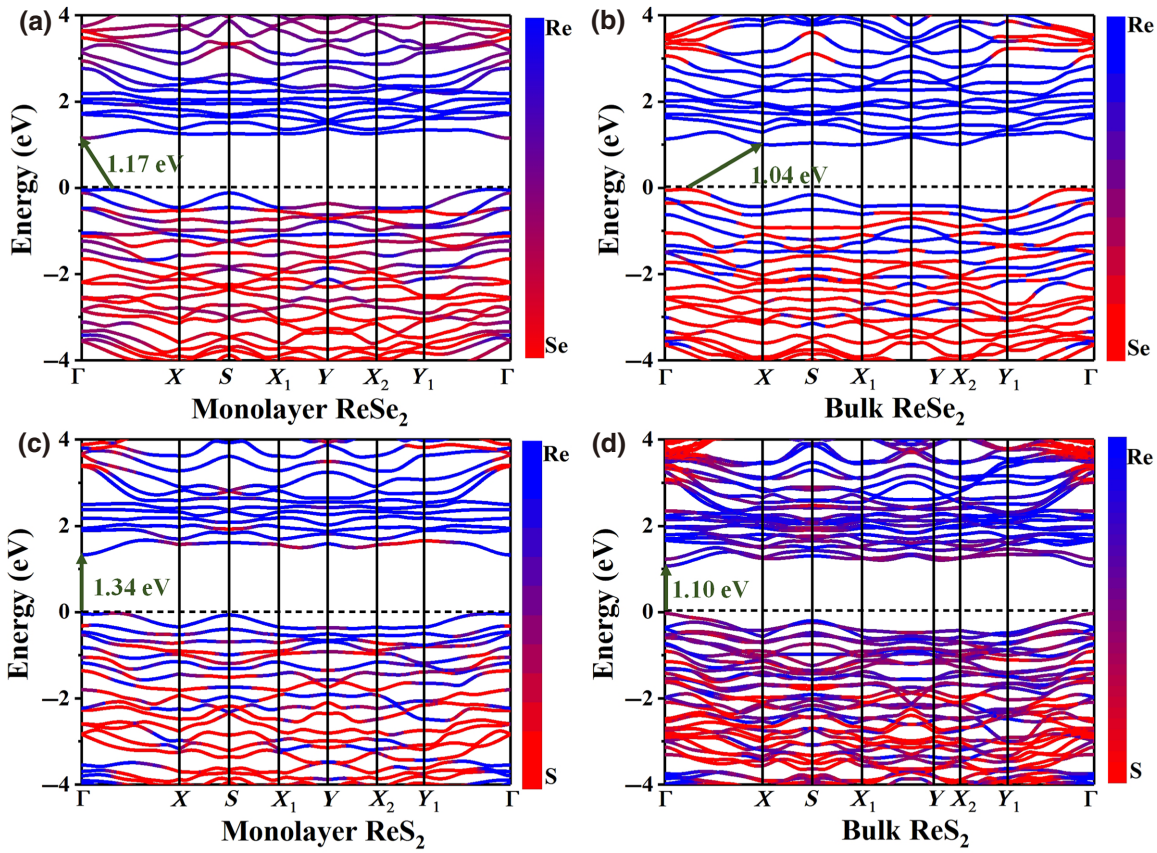

FIG. 5. Electronic band structures of ReX_2: (a) monolayer $ReSe_2$, (b) bulk $ReSe_2$, (c) monolayer ReS_2, (d) bulk ReS_2. The transition metal Re is represented in blue and chalcogen X (X = Se, S) is represented in red.

larger than the band gap of ReX_2, the SA process occurs when the interband transitions are blocked due to the Pauli exclusion principle (illustrated in Fig. S6 in the Supplemental Material [43]). Once the SA takes place ($I > I_S$, where I_S is the saturable absorption intensity), the total absorption can be expressed by $\alpha(I) = \alpha_0/(1 + I/I_S)$ [6]. Thus, the pump-intensity-dependent NLO absorption is well explained.

Secondly, the layer dependence of the nonlinear absorption of ReX_2 is also investigated at a fixed pump intensity of 393 GW/cm^2 (the Z-scan traces are shown in Fig. S7 in the Supplemental Material [43]). As the layer number increases, the normalized transmittance at the beam focus ($Z = 0$) rises gradually. By fitting the experimental data using Eq. (1), the β values of ReX_2 films are obtained and shown in Fig. 4(e). The layer number dependence of β can be fitted by the power law $\beta = A + B \times (1/L)$. Moreover, the imaginary part of the third-order NLO susceptibility is calculated by [49] $\mathrm{Im}\chi^{(3)}(\mathrm{esu}) = 10^{-7} c\lambda n^2 \beta/96\pi^2$, where λ represents incident light wavelength; c and n stand for the velocity of light in vacuum and linear refractive index, respectively. Figure 4(f) shows that the values of $\mathrm{Im}\chi^{(3)}$ exhibit a similar trend of change as β. In this experiment, the 1L $ReSe_2$ film has the most significant absolute values of β (approximately 4156 cm/GW) and $\mathrm{Im}\chi^{(3)}$ (approximately 1.15×10^{-7} esu), which declines by more than half at less than around 10 layers and then shows a saturation trend. Similarly, the 4L ReS_2 film exhibits higher β (approximately 806 cm/GW) and $\mathrm{Im}\chi^{(3)}$ (approximately 3.09×10^{-8} esu) values than those of 55L ReS_2 film ($\beta \sim 561$ cm/GW, $\mathrm{Im}\chi^{(3)} \sim 2.15 \times 10^{-8}$ esu). The weakened nonlinear absorption in thicker films can be attributed to increased defects on the grain boundaries, which trap more photons and enhance the nonlinear scattering and energy loss [50].

In Table I, we list the previously mentioned NLO parameters of ReX_2 together with the reported data of many other 2D materials. Additionally, the figure of merit ($\mathrm{FOM_{IM}}$), defined as $\mathrm{FOM_{IM}} = |\mathrm{Im}\chi^{(3)}/\alpha_0|$, is introduced to remove the discrepancy from linear absorption [10]. Compared with the β of the other 2D materials, ReX_2 films show giant nonlinear absorption properties. The $\mathrm{FOM_{IM}}$ values of ReX_2 films are in the scale of 10^{-13} esu cm, which is 10–100 times larger than those of many common 2D materials, such as approximately 3.1×10^{-14} esu cm for graphene, approximately 16.3×10^{-14} esu cm for BP, approximately 8.55×10^{-15} esu cm for WS_2, and approximately 4.6×10^{-14} esu cm for MoS_2. Note that the NLO

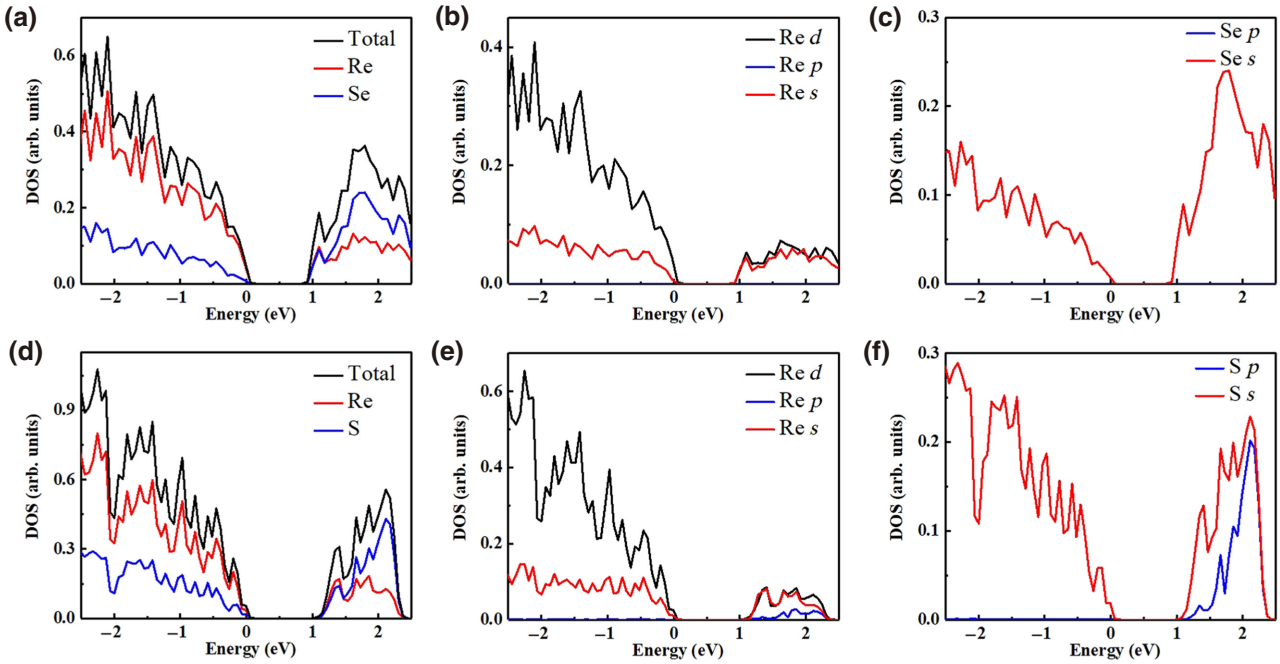

FIG. 6. DOS of (a) bulk $ReSe_2$, (b) Re, and (c) Se atoms. DOS of (d) bulk ReS_2, (e) Re, and (f) S atoms.

absorption parameters of ReS_2 are much lower than those of $ReSe_2$. The reason could be related to the smaller band gap [57,58], a higher carrier density [59], and a larger ground-state absorption [60] in $ReSe_2$ than in ReS_2.

Thirdly, to better understand the fundamental difference in the nonlinear absorption between $ReSe_2$ and ReS_2, the electronic structures of monolayer and bulk ReX_2 are studied by the density functional theory. Figures 5(a) and 5(b) show the band structures of monolayer and bulk $ReSe_2$, and Figs. 5(c) and 5(d) exhibit those of monolayer and bulk ReS_2. The bands are decomposed into transition metal (Re) and chalcogen (Se or S) atoms, which are marked with blue and red. For monolayer and bulk $ReSe_2$, the conduction band minimum is located at the high symmetry point Γ and X, respectively. The valence band maximum is located between the high symmetry point X and the high symmetry point Γ. The band gaps of $ReSe_2$ are 1.17 eV in the monolayer structure and 1.04 eV in the bulk structure, respectively. Unlike $ReSe_2$, ReS_2 is a direct-band-gap semiconductor where the conduction band minimum and the valence band maximum are both located at the high symmetry point Γ. The band gaps of ReS_2 are 1.34 eV in the monolayer structure and 1.10 eV in the bulk structure, respectively. The results demonstrate that $ReSe_2$ has a smaller band gap than ReS_2 in monolayer or bulk, which is consistent with previous reports [61,62]. Owing to the lower band gap of $ReSe_2$ than ReS_2, the valence band electrons could be excited into higher conduction band positions under the same pump photon energy of 1.55 eV. Under the same pump power, more photoexcited electrons in $ReSe_2$ can be provided than in ReS_2 due to the higher absorption efficiency in $ReSe_2$, as shown in Figs. 3(b) and 3(d), to fill the empty states of $ReSe_2$, thus resulting in a higher SA response.

TABLE II. The physical parameters based on the slow saturable absorber model.

Absorber		σ_{gs} (10^{-17} cm^2)	σ_{es} (10^{-18} cm^2)	N (10^{22} cm^{-3})	σ_{es}/σ_{gs}
$ReSe_2$	1L	2.88	7.57	7.75	0.26
	3L	1.66	0.29	7.47	0.02
	4L	1.60	0.17	5.99	0.01
ReS_2	4L	5.90	23.52	1.05	0.40
	5L	2.11	10.42	2.48	0.49
	7L	2.30	1.78	1.95	0.09

Furthermore, the local density of states (DOS) for bulk ReX_2 is calculated to analyze the carrier transition process. The DOS results of $ReSe_2$ are shown in Figs. 6(a) and 6(c). The results suggest that the bottom of the conduction band is contributed by the Se s orbital and slightly contributed by the Re d orbital. At the same time, the valence band mainly consists of the Re d orbital. Therefore, we could put forth the possible electron transition pathways: After absorbing a photon with an energy of 1.55 eV, the electron leaps from the valence band composed of Re d orbitals into the conduction band formed of mixed Re d and Se s orbitals; subsequently, the electron may leap into a higher Se s orbital by absorbing another

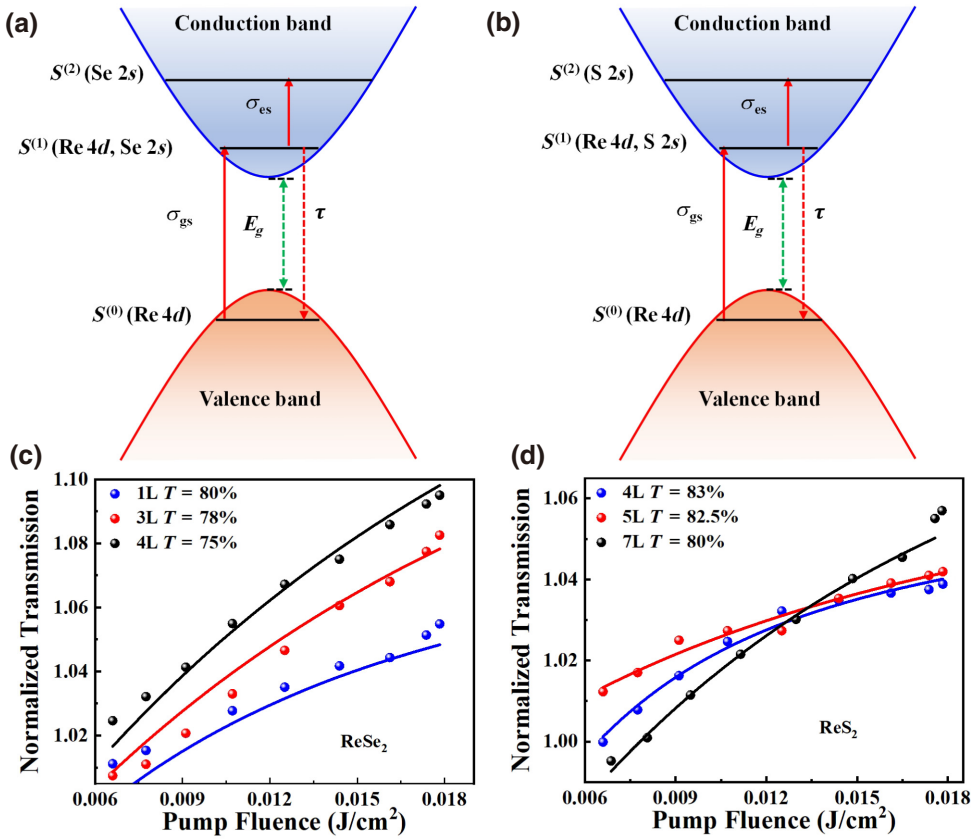

FIG. 7. The three-level system used to model the SA processes in (a) $ReSe_2$ and (b) ReS_2. Nonlinear fitting with slow saturable absorber model for (c) 1L, 3L, and 4L $ReSe_2$ films and (d) 4L, 5L, and 7L ReS_2 films.

photon, or decay to the valence band composed of Re d orbitals.

A similar discussion is made for the DOS of bulk ReS_2, which is shown in Figs. 6(d) and 6(f). The results show that the conduction band mainly comes from the S s orbital and the Re d orbital, while the valence band is dominated by the Re d orbital. Note that the S s orbital primarily contributes to the higher states of the conduction band. Herein, the transitions in bulk ReS_2 mainly occur from the valence band composed of Re d orbitals to the conduction band formed of mixed Re d and S s orbitals. Then, the electron may leap into a higher S s orbital by absorbing another photon or decay to the valence band composed of Re d orbitals. In addition, we also investigate the DOS of monolayer ReX_2 in Fig. S8 (Supplemental Material [43]; for the calculation method see Refs. [63–66]). The results of monolayer sample imply the same transition processes as those of bulk materials.

At the end of this section, we provide a deeper insight into the SA mechanism of ReX_2 with more parameters such as carrier density and absorption cross section. A three-level system is established according to the previously mentioned electron transition process of ReX_2, as shown in Figs. 7(a) and 7(b). $S^{(0)}$, $S(1)$, and $S(2)$ mark the ground state, first excited state, and high excited state of ReX_2, respectively. The probabilities of the electron transition from $S^{(0)}$ into $S^{(1)}$ and from $S^{(1)}$ into $S^{(2)}$ are determined by the absorption cross section of the ground state (σ_{gs}) and excited state (σ_{es}), respectively. The effective spontaneous decay time τ of ReX_2 is reported to be in the picosecond scale [61,67], which is far longer than the excitation pulse duration (35 fs). Therefore, the SA

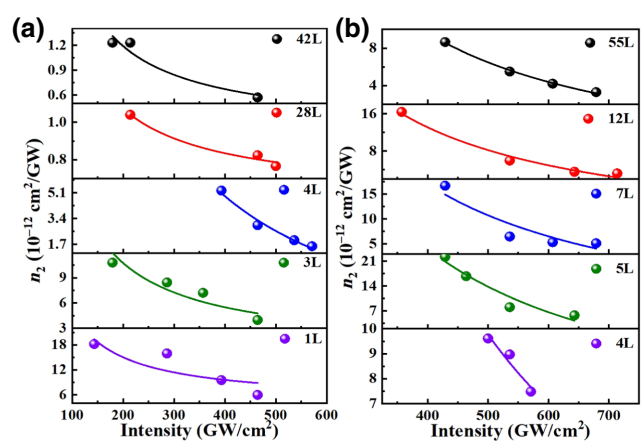

FIG. 8. n_2 values of (a) $ReSe_2$ and (b) ReS_2 films fitted by a power law.

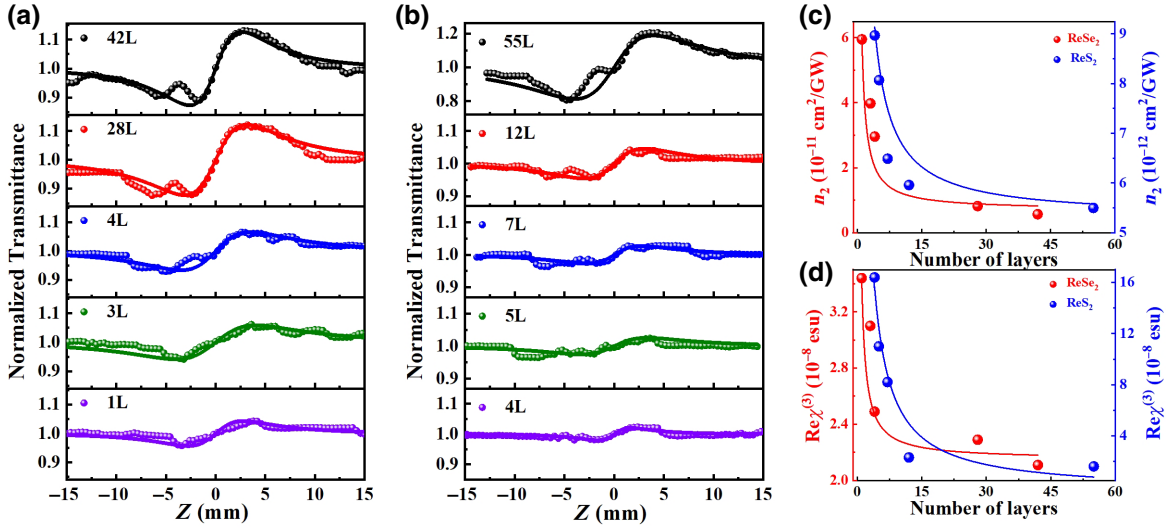

FIG. 9. CA Z-scan results of (a) $ReSe_2$ and (b) ReS_2 films with different numbers of layers at 464 and 536 GW/cm^2, respectively. (c) n_2 and (d) Re$\chi^{(3)}$ values of the $ReSe_2$ and ReS_2 films fitted by a power law.

responses of ReX_2 can be analyzed by the slow saturable absorber model [60]. Figures 7(c) and 7(d) show the fitting results of ReX_2 using the Frantz-Nodvik equation [60,68] based on the slow saturable absorber model (calculation details are in the Supplemental Material [43]). Table II lists the calculated physical parameters. The obtained carrier density N of $ReSe_2$ is 3–6 times larger than that of ReS_2, and the ratios of σ_{es}/σ_{gs} for $ReSe_2$ are smaller than those of ReS_2 films according to the three-level model. These results demonstrate a higher carrier density and a more substantial ground-state absorption in $ReSe_2$ than in ReS_2, which could be responsible for the stronger NLO absorption of $ReSe_2$ [59,60].

C. Nonlinear refraction properties of ReX_2 films

The nonlinear refraction properties of ReX_2 films are characterized by the CA Z-scan method. Firstly, the normalized Z-scan results for $ReSe_2$ and ReS_2 films at different pump intensities are shown in Figs. S9 and S10 in the Supplemental Material [43]. All the Z-scan traces of these ReX_2 films exhibit a similar shape transition from valley to peak, indicating the optical self-focusing phenomena (corresponding to positive n_2 values). By fitting the CA data with Eq. (2), the pump-intensity-dependence of n_2 for $ReSe_2$ and ReS_2 films are obtained and shown in Figs. 8(a) and 8(b), respectively. For both $ReSe_2$ and ReS_2 films, the values of n_2 decrease with the pump intensity, which can be phenomenologically fitted by the power law $n_2 = A + B \times (1/I)$. For $ReSe_2$ films with 1L, 3L, 4L, 28L, and 42L, the values of n_2 are 1.82×10^{-10}, 1.08×10^{-10}, 5.25×10^{-11}, 1.04×10^{-11}, and 1.52×10^{-11} cm^2/W, respectively. Similarly, the values of n_2 are 9.61×10^{-12}, 2.22×10^{-11}, 1.67×10^{-11}, 1.64×10^{-11}, and 8.65×10^{-12} cm^2/W for 4L, 5L, 7L, 12L, and 55L ReS_2 films, respectively.

The pump-intensity-dependent n_2 of ReX_2 films is related to the free carrier and bound electron by $n_2 = n_2^* + \sigma_\gamma N(t)/I$ [69], where n_2^* represents the effective nonlinear refractive index; $N(t)$ and σ_γ stand for photoexcited carrier density and free-carrier refraction coefficient, respectively. Therefore, when the pump intensities for $ReSe_2$ (ReS_2) are larger than approximately 110 GW/cm^2 (210 GW/cm^2), electrons in the valence band would be depleted because of SA, thus weakening the influence of bound electrons on the nonlinearity [70]. At the same time, the free-carrier density remains relatively stable [70], so the nonlinear refractive index decreases with the increase of incident light intensity.

The CA Z-scan results for $ReSe_2$ and ReS_2 films with different numbers of layers at a fixed pump intensity are shown in Figs. 9(a) and 9(b). As the layer of ReX_2 films increases, the self-focusing phenomenon gets stronger. The values of n_2 for ReX_2 films are obtained by using Eq. (2) and shown in Fig. 9(c). The fitting curves show that the values of n_2 for both $ReSe_2$ and ReS_2 decrease with the increased layer number as the power law $n_2 = A + B \times (1/L)$. The reduction of n_2 in the multilayer film could be related to the increased number of defects in the grain boundaries, which could capture more photons and decrease the number of photoexcited carriers. Moreover, compared with ReS_2, $ReSe_2$ exhibits a much stronger nonlinear refraction property. The n_2 value of $ReSe_2$ is 2–3 times larger than that of ReS_2 with a similar number of layers. This difference may be attributed to the higher carrier density in $ReSe_2$ than in ReS_2 [59]. Additionally, Fig. 9(d) shows the calculated real part of the third-order NLO susceptibility (Re$\chi^{(3)}$) of these ReX_2 films according

TABLE III. n_2 and Re$\chi^{(3)}$ of various 2D layered materials.

Sample	Number of layers	Laser Parameters	n_2 (10^{-12} cm^2/W)	Re$\chi^{(3)}$ (10^{-8} esu)	Ref.
$ReSe_2$	1L	800 nm 35 fs 1 kHz	59.5	16.4	This work
	3L		39.8	11	
	4L		29.6	8.2	
	28L		8.24	2.3	
	42L		5.72	1.6	
ReS_2	4L		8.97	3.44	
	5L		8.07	3.1	
	7L		6.49	2.49	
	12L		5.96	2.29	
	55L		5.50	2.11	
Si	–	1540 nm 220 fs	0.045	–	[71]
GaAs	–		0.159	–	[71]
WS_2	0.75 nm	1040 nm 340 fs 100 Hz	128 ± 3	0.48 ± 0.012	[72]
WS_2	20 μm	1064 nm 25 ps 20 Hz	58.3 ± 1.8	2.31 ± 0.21	[51]
WS_2/PMMA	0.27 mm	800 nm 130 fs	0.334	4.7×10^{-4}	[73]
MoS_2	~25 μm	1064 nm 25 ps 20 Hz	1.88 ± 0.48	$(8.71 \pm 1.59) \times 10^{-2}$	[51]
MoS_2	–	800 nm 100 fs 1 kHz	$(4.5 \pm 0.3) \times 10^{-4}$	–	[74]
$MoSe_2$	2L–3L	1064 nm 4 ns 10 Hz	0.2	8.2×10^{-4}	[75]
$MoSe_2$/graphene	–	532 nm 30 ps 10 Hz	1.34×10^{-2}	7.84×10^{-4}	[76]
Bi_2Se_3	50 nm	800 nm 100 fs 1 kHz	226	–	[69]
1% Bi_2S_3/glass	–	770 nm fs	2.56	0.0142	[77]
Sb_2S_3	–	532 nm 4.5 ns	0.632	–	[78]
Bi_2S_3	–	532 nm 4.5 ns	0.855	–	[78]
NbS_2	1.36 ± 0.5 nm	800 nm 100 fs 1 kHz	$(3 \pm 0.2) \times 10^{-4}$	–	[74]
Glass	–	800 nm 150 fs 80 MHz	0.132 ± 0.013	–	[79]
$CsPbBr_3$	–	800 nm 70 fs 1 kHz	3.52	–	[80]
BiOCl	20–140 nm	800 nm 100 fs 1 kHz	38	–	[70]
Graphene	5L–7L	1150 nm 100 fs 1 kHz	$\sim 10^3$	–	[8]
GO	1 μm	1150 nm 67 fs 20 MHz	450	–	[81]
GO	2 μm	800 nm 100 fs	1250	–	[82]
BP	30–60 nm	800 nm 100 fs	6800	–	[11]
BiOBr	140 nm	1550 nm 140 fs	382.4	–	[82]

GO, graphene oxide.

to Re $\chi^{(3)}$(esu) $= [10^{-7}\ cn^2/48\pi^2]n_2$(cm^2/W). The layer dependence of Re$\chi^{(3)}$ shows a similar trend as n_2.

Finally, we list the nonlinear refraction parameters of these ReX_2 films with different numbers of layers in Table III, combined with the previously reported parameters of other 2D materials. The results show that ReX_2 has a considerable nonlinear refraction response. The values of n_2 are 3–4 orders of magnitude larger than conventional semiconductors such as Si and GaAs [71]. Compared with many other layered materials, such as Bi_2S_3 [78], MoS_2 [51,74], $MoSe_2$ [75], and NbS_2 [74], the parameters of n_2 and Re$\chi^{(3)}$ are also 1–2 orders of magnitude higher. As a result, ReX_2 films may also be promising for self-focusing applications in nanophotonic devices such as the all-optical switch.

V. CONCLUSIONS

A series of high-quality ReX_2 films with controllable numbers of layers are prepared by the CVD method. In the Z-scan experiment, these films exhibit giant NLO responses at 800 nm. The absolute values of β and n_2 decrease with the increase of layer number and pump intensity as the power exponential function. The absolute value of β for $ReSe_2$ (−4156 cm/GW) is larger than that of ReS_2 (−806 cm/GW), and the n_2 of $ReSe_2$ (1.819×10^{-10} cm^2/W) is also larger than that of ReS_2 (2.22×10^{-11} cm^2/W). The detailed theoretical analysis suggests that the larger NLO response of $ReSe_2$ films is due to a smaller band gap, a higher carrier density, and a higher ground-state absorption of $ReSe_2$ films. These results pave the way for selecting suitable NLO materials and appropriate layers for future photonic device applications.

ACKNOWLEDGMENTS

This work was supported by National Natural Science Foundation of China (Grants No. 12074311, No. 11974279, No. 62004162).

[1] M. E. Maldonado, A. Das, A. M. Jawaid, A. J. Ritter, R. A. Vaia, D. A. Nagaoka, P. G. Vianna, L. Seixas, C. J. S. de Matos, A. Baev, *et al.*, Nonlinear optical interactions and relaxation in 2D layered transition metal dichalcogenides probed by optical and photoacoustic *Z*-scan methods, ACS Photonics **7**, 3440 (2020).

[2] R. L. Sutherland, *Handbook of Nonlinear Optics* (2003).

[3] S. G. L. Robert, W. Boyd, and Y. R. Shen, *Self-focusing: Past and Present*. Vol. 114 (Self-focusing: Past and Present, 2009).

[4] V. A. Maslov, V. A. Mikhailov, O. P. Shaunin, and I. A. Shcherbakov, Nonlinear absorption in KTP crystals, Quantum Electron. **27**, 356 (1997).

[5] R. A. Ganeev, I. A. Kulagin, A. I. Ryasnyansky, R. I. Tugushev, and T. Usmanov, Characterization of nonlinear optical parameters of KDP, $LiNbO_3$ and BBO crystals, Opt. Commun. **229**, 403 (2004).

[6] G. Wang, A. A. Baker-Murray, and W. J. Blau, Saturable absorption in 2D nanomaterials and related photonic devices, Laser Photonics Rev. **13**, 1800282 (2019).

[7] B. Zhang, J. Liu, C. Wang, K. Yang, C. Lee, H. Zhang, and J. He, Recent progress in 2D material-based saturable absorbers for all solid-state pulsed bulk lasers, Laser Photonics Rev. **14**, 1900240 (2019).

[8] G. Demetriou, H. T. Bookey, F. Biancalana, E. Abraham, Y. Wang, W. Ji, and A. K. Kar, Nonlinear optical properties of multilayer graphene in the infrared, Opt. Express **24**, 13033 (2016).

[9] M. He, C. Quan, C. He, Y. Huang, L. Zhu, Z. Yao, S. Zhang, J. Bai, and X. Xu, Enhanced nonlinear saturable absorption of MoS_2/graphene nanocomposite films, J. Phys. Chem. C **121**, 27147 (2017).

[10] R. Chen, Y. Tang, X. Zheng, and T. Jiang, Giant nonlinear absorption and excited carrier dynamics of black phosphorus few-layer nanosheets in broadband spectra, Appl. Opt. **55**, 10307 (2016).

[11] X. Zheng, R. Chen, G. Shi, J. Zhang, Z. Xu, X. Cheng, and T. Jiang, Characterization of nonlinear properties of black phosphorus nanoplatelets with femtosecond pulsed *Z*-scan measurements, Opt. Lett. **40**, 3480 (2015).

[12] G. Wang, A. A. Baker-Murray, X. Zhang, D. Bennett, J. J. Wang, J. Wang, K. Wang, and W. J. Blau, Broadband saturable absorption and exciton-exciton annihilation in $MoSe_2$ composite thin films, Opt. Mater. Express **9**, 483 (2019).

[13] S. Zhang, N. Dong, N. McEvoy, M. O'Brien, S. Winters, N. C. Berner, C. Yim, Y. Li, X. Zhang, Z. Chen, *et al.*, Direct observation of degenerate two-photon absorption and its saturation in WS_2 and MoS_2 monolayer and few-layer films, ACS Nano **9**, 7142 (2015).

[14] C. Lu, C. Quan, K. Si, X. Xu, C. He, Q. Zhao, Y. Zhan, and X. Xu, Charge transfer in graphene/WS_2 enhancing the saturable absorption in mixed heterostructure films, Appl. Surf. Sci. **479**, 1161 (2019).

[15] G. Liang, L. Zeng, Y. H. Tsang, L. Tao, C. Y. Tang, P. K. Cheng, H. Long, X. Liu, J. Li, J. Qu, and Q. Wen, Technique and model for modifying the saturable absorption (SA) properties of 2D nanofilms by considering interband exciton recombination, J. Mater. Chem. C **6**, 7501 (2018).

[16] L. Wang, S. Zhang, N. McEvoy, Y. Y. Sun, J. Huang, Y. Xie, N. Dong, X. Zhang, I. M. Kislyakov, J. M. Nunzi, *et al.*, Nonlinear optical signatures of the transition from semiconductor to semimetal in $PtSe_2$, Laser Photonics Rev. **13**, 1900052 (2019).

[17] H. Zhang, S. B. Lu, J. Zheng, J. Du, S. C. Wen, D. Y. Tang, and K. P. Loh, Molybdenum disulfide (MoS_2) as a broadband saturable absorber for ultra-fast photonics, Opt. Express **22**, 7249 (2014).

[18] H. Liu, A. P. Luo, F. Z. Wang, R. Tang, M. Liu, Z. C. Luo, W. C. Xu, C. J. Zhao, and H. Zhang, Femtosecond pulse erbium-doped fiber laser by a few-layer MoS_2 saturable absorber, Opt. Lett. **39**, 4591 (2014).

[19] S. Wang, H. Yu, H. Zhang, A. Wang, M. Zhao, Y. Chen, L. Mei, and J. Wang, Broadband few-layer MoS_2 saturable absorbers, Adv. Mater. **26**, 3538 (2014).

[20] K. Friemelt, M. C. LuxSteiner, and E. Bucher, Optical properties of the layered transition-metal-dichalcogenide ReS_2: Anisotropy in the van der Waals plane, J. Appl. Phys. **74**, 5266 (1993).

[21] B. Jariwala, D. Voiry, A. Jindal, B. A. Chalke, R. Bapat, A. Thamizhavel, M. Chhowalla, M. Deshmukh, and A. Bhattacharya, Synthesis and characterization of ReS_2 and $ReSe_2$ layered chalcogenide single crystals, Chem. Mater. **28**, 3352 (2016).

[22] S. Wang, H. Huang, X. Liu, H. Chen, W. Zhou, S. Liu, and D. Shen, Rhenium diselenide as the broadband saturable absorber for the nanosecond passively Q-switched thulium solid-state lasers, Opt. Mater. **88**, 630 (2019).

[23] Z. Li, N. Dong, Y. Zhang, J. Wang, H. Yu, and F. Chen, Invited Article: Mode-locked waveguide lasers modulated by rhenium diselenide as a new saturable absorber, APL Photonics **3**, 080802 (2018).

[24] Y. Xue, L. Li, B. Zhang, R. Wang, J. Cui, F. Tian, and J. Zhang, Watt-level continuous-wave mode-locked Nd:YVO_4 laser with $ReSe_2$ saturable absorber, IEEE Photonics J. **12**, 1 (2020).

[25] J. Lee, S. Kwon, T. Kim, J. Jung, L. Zhao, and J. H. Lee, Nonlinear optical property measurements of rhenium diselenide used for ultrafast fiber laser mode-locking at1.9 μm, Sci. Rep. **11**, 9320 (2021).

[26] L. Zhou, X. Duan, W. Xie, T. Qi, Y. Yang, W. Yang, J. Yuan, Y. Shen, H. Liang, and L. Li, Optical and laser performances of a layered $ReSe_2$ saturable absorber for a 2-μm solid laser, Opt. Laser Technol. **135**, 106685 (2021).

[27] N. Wang, B. Lu, X. Qi, Y. Jiao, Z. Wen, H. Chen, and J. Bai, Passively Q-switched ytterbium-doped fiber laser with $ReSe_2$ saturable absorber, Opt. Laser Technol. **116**, 300 (2019).

[28] C. Li, Y. Leng, and J. Huo, Diode-pumped solid-state Q-switched laser with rhenium diselenide as saturable absorber, Appl. Sci. **8**, 1753 (2018).

[29] Y. Xue, L. Li, B. Zhang, R. Wang, H. Tian, J. Cui, F. Tian, and J. Zhang, $ReSe_2$ passively Q-switched Nd : $Y_3Al_5O_{12}$ laser with near repetition rate limit ofmicrosecond pulse output, Opt. Commun. **445**, 165 (2019).

[30] Chun Li, Yuxin Leng, and Jinjin Huo, $ReSe_2$ as a saturable absorber in a Tm-doped yttrium lithium fluoride (Tm:YLF) pulse laser, Chin. Opt. Lett. **17**, 011402 (2019).

[31] Y. Yao, X. Li, R. Song, N. Cui, S. Liu, H. Zhang, D. Li, Q. Wang, Y. Xu, and J. He, The energy band structure analysis and 2 μm Q-switched laser application of layered rhenium diselenide, RSC Adv. **9**, 14417 (2019).

[32] D. Mao, X. Cui, X. Gan, M. Li, W. Zhang, H. Lu, and J. Zhao, Passively Q-switched and mode-locked fiber laser based on an ReS_2 saturable absorber, IEEE J. Sel. Top. Quantum Electron. **24**, 1 (2018).

[33] F. Lu, Passively harmonic mode-locked fiber laser based on ReS_2 saturable absorber, Mod. Phys. Lett. B **31**, 1750206 (2017).

[34] X. Xu, M. He, C. Quan, R. Wang, C. Liu, Q. Zhao, Y. Zhou, J. Bai, and X. Xu, Saturable absorption properties of ReS_2 films and mode-locking application based on double-covered ReS_2 micro-fiber, J. Lightwave Technol. **36**, 5130 (2018).

[35] Y. Cui, F. Lu, and X. Liu, Nonlinear saturable and polarization-induced absorption of rhenium disulfide, Sci. Rep. **7**, 40080 (2017).

[36] S. Han, S. Zhou, X. Liu, Y. Liu, S. Zhang, and X. Yang, Rhenium disulfide-based passively Q-switched dual-wavelength laser at 0.95 μm and 1.06 μm in Nd:YAG, Laser Phys. Lett. **15**, 085804 (2018).

[37] N. Zhang, Z. Zeng, Z. Wang, B. Li, and Y. Pan, Nd:YSAG Q-switched laser with anisotropic ReS_2 nanosheets, Optik **208**, 164542 (2020).

[38] S. Liu, M. Wang, S. Yin, Z. Xie, Z. Wang, S. Zhou, and P. Chen, Nonlinear optical properties of few-layer rhenium disulfide nanosheets and their passively Q-switched laser application, Phys. Status Solidi A **216**, 1800837 (2019).

[39] M. Lin, Q. Peng, W. Hou, X. Fan, and J. Liu, 1.3 μm Q-switched solid-state laser based on few-layer ReS_2 saturable absorber, Opt. Laser Technol. **109**, 90 (2019).

[40] X. Xu, M. Jiang, D. Li, R. Wang, Z. Ren, and J. Bai, Passive Q-switching based on ReS_2 saturable absorber in Er-doped fiber laser at 1532 nm, Opt. Quantum Electron. **50**, 39 (2018).

[41] K. Wu, B. Chen, S. Yang, G. Wang, W. Kong, H. Cai, T. Aoki, E. Soignard, X. Marie, A. Yano, *et al.*, Domain architectures and grain boundaries in chemical vapor deposited highly anisotropic ReS_2 monolayer films, Nano Lett. **16**, 5888 (2016).

[42] F. Cui, X. Li, Q. Feng, J. Yin, L. Zhou, D. Liu, K. Liu, X. He, X. Liang, and S. Liu, Epitaxial growth of large-area and highly crystalline anisotropic $ReSe_2$ atomic layer, Nano Res. **10**, 2732 (2017).

[43] See Supplemental Material at http://link.aps.org/supplemental/10.1103/PhysRevApplied.18.034050 for more experimental results.

[44] X. Li, F. Cui, Q. Feng, G. Wang, X. Xu, J. Wu, N. Mao, X. Liang, Z. Zhang, J. Zhang, and H. Xu, Controlled growth of large-area anisotropic ReS_2 atomic layer and its photodetector application, Nanoscale **8**, 18956 (2016).

[45] S. Jiang, Z. Zhang, N. Zhang, Y. Huan, Y. Gong, M. Sun, J. Shi, C. Xie, P. Yang, Q. Fang, *et al.*, Application of chemical vapor–deposited monolayer $ReSe_2$ in the electrocatalytic hydrogen evolution reaction, Nano Res. **11**, 1787 (2018).

[46] F. Liu, S. Zheng, X. He, A. Chaturvedi, J. He, W. L. Chow, T. R. Mion, X. Wang, J. Zhou, Q. Fu, *et al.*, Highly sensitive detection of polarized light using anisotropic 2D ReS_2, Adv. Funct. Mater. **26**, 1169 (2016).

[47] M. Sheik-Bahae, A. A. Said, T.-H. Wei, D. J. Hagan, and E. W. V. Stryland, Sensitive measurement of optical nonlinearities using a single beam, IEEE J. Quantum Electron. **26**, 760 (1990).

[48] C. Lu, M. Luo, Y. Ge, Y. Huang, Q. Zhao, Y. Zhou, and X. Xu, Layer-dependent nonlinear optical properties of WS_2, MoS_2, and Bi_2S_3 films synthesized by chemical vapor deposition, ACS Appl. Mater. Interfaces **14**, 2390 (2022).

[49] K. Wang, J. Wang, J. Fan, M. Lotya, A. O'Neill, D. Fox, Y. Feng, X. Zhang, B. Jiang, Q. Zhao, *et al.*, Ultrafast saturable absorption of two-dimensional MoS_2 nanosheets, ACS Nano **7**, 9260 (2013).

[50] J. Zhang, T. Jiang, X. Zheng, C. Shen, and X. Cheng, Thickness-dependent nonlinear optical properties of $CsPbBr_3$ perovskite nanosheets, Opt. Lett. **42**, 3371 (2017).

[51] S. Bikorimana, P. Lama, A. Walser, R. Dorsinville, S. Anghel, A. Mitioglu, A. Micu, and L. Kulyuk, Nonlinear optical responses in two-dimensional transition metal dichalcogenide multilayer: WS_2, WSe_2, MoS_2 and $Mo_{0.5}W_{0.5}S_2$, Opt. Express **24**, 20685 (2016).

[52] C. Quan, C. Lu, C. He, X. Xu, Y. Huang, Q. Zhao, and X. Xu, Band alignment of $MoTe_2/MoS_2$ nanocomposite films for enhanced nonlinear optical performance, Adv. Mater. Interfaces **6**, 1801733 (2019).

[53] R. Chen, X. Zheng, and T. Jiang, Broadband ultrafast nonlinear absorption and ultra-long exciton relaxation time of black phosphorus quantum dots, Opt. Express **25**, 7507 (2017).

[54] G. Wang, K. Wang, N. McEvoy, Z. Bai, C. P. Cullen, C. N. Murphy, J. B. McManus, J. J. Magan, C. M. Smith, G. S. Duesberg, *et al.*, Ultrafast carrier dynamics and bandgap renormalization in layered $PtSe_2$, Small **15**, 1902728 (2019).

[55] C. Liu, L. Cheng, Y. Yuan, J. Su, X. Zhang, X. Li, H. Zhao, H. Zhang, Y. Zheng, and J. Li, Contrastive investigation on linear optical properties and nonlinear absorption behaviors between Sb_2Se_3 and Sb_2Te_3 thin films, Mater. Res. Express **6**, 086446 (2019).

[56] J. Wang, F. Jin, X. Cao, S. Cheng, C. Liu, Y. Yuan, J. Fang, H. Zhao, and J. Li, In_2Te_3 thin films: A promising nonlinear optical material with tunable nonlinear absorption response, RSC Adv. **6**, 103357 (2016).

[57] Y. Zhou, Y. Huang, X. Xu, Z. Fan, J. B. Khurgin, and Q. Xiong, Nonlinear optical properties of halide perovskites and their applications, Appl. Phys. Rev. **7**, 041313 (2020).

[58] A. Taghizadeh, K. S. Thygesen, and T. G. Pedersen, Two-dimensional materials with giant optical nonlinearities near the theoretical upper limit, ACS Nano **15**, 7155 (2021).

[59] C. Ye, Z. Yang, J. Dong, Y. Huang, M. Song, B. Sa, J. Zheng, and H. Zhan, Layer-tunable nonlinear optical characteristics and photocarrier dynamics of 2D $PdSe_2$ in broadband spectra, Small **17**, 2103938 (2021).

[60] S. Zhang, Y. Li, X. Zhang, N. Dong, K. Wang, D. Hanlon, J. N. Coleman, L. Zhang, and J. Wang, Slow and fast absorption saturation of black phosphorus: experiment and modelling, Nanoscale **8**, 17374 (2016).

[61] S. Jiang, J. Yang, Y. Shi, J. Zhao, C. Xie, L. Zhao, J. Fu, P. Yang, Y. Huan, Q. Xie, *et al.*, Salt-assisted growth and

ultrafast photocarrier dynamics of large-sized monolayer $ReSe_2$, Nano Res. **13**, 667 (2020).

[62] H.-X. Zhong, S. Gao, J.-J. Shi, and L. Yang, Quasiparticle Band Gaps, Excitonic Effects, and Anisotropic Optical Properties of the Monolayer Distorted 1T Diamond-Chain Structures ReS_2 and $ReSe_2$, Phys. Rev. B **92**, 115438 (2015).

[63] M. Dion, H. Rydberg, E. Schröder, D. C. Langreth, and B. I. Lundqvist, Van der Waals Density Functional for General Geometries, Phys. Rev. Lett. **92**, 246401 (2004).

[64] M. Ernzerhof and G. E. Scuseria, Assessment of the Perdew–Burke–Ernzerhof exchange-correlation functional, J. Chem. Phys. **110**, 5029 (1999).

[65] A. D. Becke, Density-Functional Exchange-Energy Approximation with Correct Asymptotic Behavior, Phys. Rev. A **38**, 3098 (1988).

[66] H. J. Monkhorst and J. D. Pack, Special Points for Brillouin-Zone Integrations, Phys. Rev. B **13**, 5188 (1976).

[67] S. Sim, D. Lee, J. Lee, H. Bae, M. Noh, S. Cha, M. H. Jo, K. Lee, and H. Choi, Light polarization-controlled conversion of ultrafast coherent-incoherent exciton dynamics in few-layer ReS_2, Nano Lett. **19**, 7464 (2019).

[68] M. Pokrass, Z. Burshtein, R. Gvishi, and M. Nathan, Saturable absorption of multi-walled carbon nanotubes/hybrid-glass composites, Opt. Mater. Express **2**, 825 (2012).

[69] S. Lu, C. Zhao, Y. Zou, S. Chen, Y. Chen, Y. Li, H. Zhang, S. Wen, and D. Tang, Third order nonlinear optical property of Bi_2Se_3, Opt. Express **21**, 2072 (2013).

[70] R. Chen, X. Zheng, Y. Zhang, Y. Tang, and T. Jiang, *Z*-scan measurement of nonlinear optical properties of BiOCl nanosheets, Appl. Opt. **54**, 6592 (2015).

[71] M. Dinu, F. Quochi, and H. Garcia, Third-order nonlinearities in silicon at telecom wavelengths, Appl. Phys. Lett. **82**, 2954 (2003).

[72] N. Dong, Y. Li, S. Zhang, N. McEvoy, X. Zhang, Y. Cui, L. Zhang, G. S. Duesberg, and J. Wang, Dispersion of nonlinear refractive index in layered WS_2 and WSe_2 semiconductor films induced by two-photon absorption, Opt. Lett. **41**, 3936 (2016).

[73] R. Wei, X. Tian, H. Zhang, Z. Hu, X. He, Z. Chen, Q. Chen, and J. Qiu, Facile synthesis of two-dimensional WS_2 with reverse saturable absorption and nonlinear refraction properties in the PMMA matrix, J. Alloys Compd. **684**, 224 (2016).

[74] M. Maldonado, M. L. da Silva Neto, P. G. Vianna, H. B. Ribeiro, V. O. Gordo, I. C. S. Carvalho, L. S. de Menezes, C. B. de Araújo, C. J. S. de Matos, L. Seixas, *et al.*, Femtosecond nonlinear optical properties of 2D metallic NbS_2 in the near infrared, J. Phys. Chem. C **124**, 15425 (2020).

[75] H. Pan, H. Chu, Y. Li, S. Zhao, and D. Li, Comprehensive study on the nonlinear optical properties of few-layered $MoSe_2$ nanosheets at 1 μm, J. Alloys Compd. **806**, 52 (2019).

[76] G. Liu, S. Dai, B. Zhu, P. Li, Z. Wu, and Y. Gu, Third-order nonlinear optical properties of $MoSe_2$/graphene composite materials, Opt. Laser Technol. **120**, 105746 (2019).

[77] X. Yang, W. Xiang, H. Zhao, X. Zhang, X. Liang, S. Dai, and F. Chen, Third-order nonlinear optical properties of Bi_2S_3 nanocrystals doped in sodium borosilicate glass studied with *Z*-scan technique, Mater. Res. Bull. **46**, 355 (2011).

[78] C. Li, G. Shi, Y. Song, X. Zhang, S. Guang, and H. Xu, Third-order nonlinear optical properties of Bi_2S_3 and Sb_2S_3 nanorods studied by the *Z*-scan technique, J. Phys. Chem. Solids **69**, 1829 (2008).

[79] G. Jagannath, B. Eraiah, K. NagaKrishnakanth, and S. Venugopal Rao, Linear and nonlinear optical properties of gold nanoparticles doped borate glasses, J. Non-Cryst. Solids **482**, 160 (2018).

[80] R. Ketavath, N. K. Katturi, S. G. Ghugal, H. K. Kolli, T. Swetha, V. R. Soma, and B. Murali, Deciphering the ultrafast nonlinear optical properties and dynamics of pristine and Ni-doped $CsPbBr_3$ colloidal two-dimensional nanocrystals, J. Phys. Chem. Lett. **10**, 5577 (2019).

[81] X. Xu, X. Zheng, F. He, Z. Wang, H. Subbaraman, Y. Wang, B. Jia, and R. T. Chen, Observation of third-order nonlinearities in graphene oxide film at telecommunication wavelengths, Sci. Rep. **7**, 9646 (2017).

[82] L. Jia, D. Cui, J. Wu, H. Feng, Y. Yang, T. Yang, Y. Qu, Y. Du, W. Hao, B. Jia, and D. J. Moss, Highly nonlinear BiOBr nanoflakes for hybrid integrated photonics, APL Photonics **4**, 090802 (2019).